

# Controllable SH wave radiation patterns generated by finite-size face-shear piezoelectric transducers for structural health monitoring

Hongchen Miao<sup>a)</sup>, Lei Xu, Hao Zhang, Guozheng Kang

Applied Mechanics and Structure Safety Key Laboratory of Sichuan Province, School of Mechanics and Engineering, Southwest Jiaotong University, Chengdu, Sichuan, 610031, China

## Abstract

The fundamental shear horizontal ( $SH_0$ ) wave in plate-like structures is of practical importance in structural health monitoring due to its non-dispersive characteristics. However, compared with Lamb wave,  $SH_0$  wave is less used in practice since it is difficult to be excited by using conventional piezoelectric transducers. Recently, face-shear piezoelectric mode has been realized in PZT ceramics and several face-shear piezoelectric transducers have been developed to excite pure  $SH_0$  wave in plates. However, when controllable radiation pattern of  $SH_0$  wave is required, it is found that no mathematical basis is available for designers to optimize the transducer's parameters. In this work, based on the reciprocal theorem of elastodynamics and Huygens' principle, a theoretical model is proposed to describe the  $SH_0$  wave field generated by arbitrary-shaped face-shear transducers bonded on an infinite isotropic plate. It is proved that the wave field generated by a face-shear transducer is equivalent to that generated by uniform in-plane tractions along its perimeter. Then the proposed model is applied to two specific cases of a single square face-shear ( $d_{24}$ ) PZT wafer and a bidirectional  $SH_0$  wave piezoelectric transducer (BSH-PT). Explicit analytical expressions for both cases are successfully obtained. The accuracy of the obtained analytical model is verified by both experiments and FEM simulations. Furthermore, some general guidelines based on the analytical model are presented for optimization of the transducer's dimensions. Finally, based on the guidelines, a new bidirectional  $SH_0$  wave piezoelectric transducer is proposed with very small beam divergence.

**Keywords:** structural health monitoring (SHM); shear horizontal waves; guided wave; piezoelectric transducer.

---

Author to whom all correspondence should be addressed, <sup>a)</sup> Email: [miaohongchen@swjtu.edu.cn](mailto:miaohongchen@swjtu.edu.cn)

## 1. Introduction

Guided-wave-based structural health monitoring (SHM) is an area of increasing interest. As an active SHM technology, it can improve the reliability of infrastructures and save the cost of unnecessary maintenance by replacing scheduled maintenance with condition-based maintenance. The transducer for guide-wave generation and reception is a key component of a SHM system. Transducers are permanently installed onto structures in SHM systems, so conventional nondestructive testing (NDT) transducers, which are typically expensive and bulky, are not feasible. Development of compact, lightweight, cost-effective and high-performance transducers is thus a key step in the path of switching from guided-wave-based NDT to SHM[1].

Piezoelectric materials are preferred in SHM due to their compact size and peculiar electromechanical coupling properties. A thickness-poled  $d_{31}$  mode PZT wafer is inherently a Lamb wave transducer, so great efforts are made to optimize transducer parameters to excite pure desired mode and control the radiation pattern of the incident wave[1, 2]. It is also expected that the magnitude of the generated wave mode is maximum, which means that the energy conversion efficiency of the transducer is high. In order to alleviate the difficulty of signal processing caused by multimodal characteristics of Lamb waves, various efforts in transducer design have been made to selectively excite a single desired mode which can mainly be classified into three types: single-transducer mode tuning technique[3-5], multi-transducer mode tuning technique[6-9] and symmetric bonding technique[10]. Actually, Lamb wave transducer arrays are usually required to diagnose defects in SHM systems[11-13], in which single mode excitation by each transducer is always desired. Giurgiutiu[3] built a model describing the Lamb wave tuning mechanism of a surface-bonded  $d_{31}$  mode PZT wafer by using integral transform method. As he suggested, pure mode Lamb wave can be excited by a PZT wafer at the tuning frequency. This technique can be expanded to multi-transducer mode tuning technique, in which multi transducers are placed with appropriate space and driven separately[2]. Raghavan and Cesnik[14] developed a 3D elasticity theory for solving Lamb wave field generated by finite-size piezoelectric transducer, which can be used to deduce optimal dimensions of the transducer and guide the mode tuning. Su et al.[10] used a pair of PZT wafers symmetrically mounted on the upper and lower surfaces of a plate to achieve the same goal. With in-phase excitation applied on the two symmetrically-mounted PZT wafers, pure  $S_0$  mode can be generated while pure  $A_0$  mode can be achieved with out-of-phase excitation.

Besides single mode excitation, controlling the radiation pattern of the incident wave is another important problem[15, 16]. Bidirectional[1, 17], unidirectional[18, 19] and omnidirectional[8, 20] Lamb wave have been achieved by various piezoelectric transducers and electromagnetic acoustic transducers. A thickness-poled  $d_{31}$  mode ring-shaped PZT wafer is inherently an omnidirectional Lamb wave transducer[7], while the interdigital transducer (IDT) is a bidirectional Lamb wave transducer[17]. Wilcox et al.[21] developed a simulation software based on Huygens' principle to predict the acoustic field excited by IDTs. It was found that the beam divergence angle  $\beta$  is given by  $\arcsin[\lambda / (2L)]$ , where  $\lambda$  is the wavelength and  $2L$  is the finger length of IDTs. Salas and Cesnik[22] developed a 3D elasticity theory for Lamb wave excitation by a wedge-shaped IDT. These models can provide a quick guideline for radiation pattern design of Lamb wave transducers.

Recently, there is an increasing interest in developing the fundamental shear horizontal ( $SH_0$ ) wave transducers, since  $SH_0$  wave is totally non-dispersive and less mode conversion will occur when it encounters defects or boundaries. Traditionally,  $SH_0$  wave can be generated by using electromagnetic acoustic transducers (EMAT)[23], which can mainly be classified into two types[24]: periodic permanent magnet (PPM) EMAT[25] and magnetostrictive EMAT[26]. However, EMAT requires high power excitation and tends to be bulky and heavy, so it is not suitable for SHM. Piezoelectric transducers are more attractive for SHM, but it is not straightforward to excite  $SH_0$  wave by conventional piezoelectric transducers. Wilcox et al.[27] employed an in-plane poled thickness-shear ( $d_{15}$ ) mode PZT wafer to excite  $SH_0$  wave. However, Lamb waves were simultaneously generated along the poling direction of the  $d_{15}$  mode PZT wafer. Belanger and Boivin[28] developed an omnidirectional  $SH_0$  wave transducer based on six in-plane poled  $d_{15}$  mode PZT patches. Zhou et al.[29] employed a  $d_{36}$  face-shear PMN-PT single crystal wafer to excite  $SH_0$  wave. However, the PMN-PT single crystal wafer cannot be widely used due to its lower Curie temperature and high cost. Miao et al.[30, 31] realized the face-shear ( $d_{36}$ ) mode in PZT ceramics via fabricating engineered ferroelectric domain and successfully excite  $SH_0$  wave in plates [32]. It should be noted that neither the  $d_{36}$  face-shear PZT nor PMN-PT single crystal wafer can excite pure  $SH_0$  wave, since the  $d_{31}$  and  $d_{33}$  modes always coexist with the  $d_{36}$  mode. Li and Miao [33] developed apparent face-shear mode ( $d_{36}$ ) piezoelectric transducers via

two-dimensional antiparallel poling. Since the face-shear deformation is synthetic, pure  $SH_0$  wave can only be excited in a narrow frequency range. Koehler et al.[34] developed a  $SH_0$  wave fiber patch transducer, which actually is also based on the principle of synthetic face-shear deformation. Ren et al.[35] recently developed a face-shear mode PVDF sensor to detect  $SH_0$  wave. More recently, Miao et al.[36] proposed a new face-shear ( $d_{24}$ ) mode piezoelectric transducer, which can generate pure  $SH_0$  wave along four main directions ( $0^\circ$ ,  $90^\circ$ ,  $180^\circ$  and  $270^\circ$ ) in a wide frequency range. Based on the face-shear ( $d_{24}$ ) PZT wafer, Miao et al. further developed omnidirectional[37] and bidirectional[16]  $SH_0$  wave piezoelectric transducers. Very recently, Huan et al.[38] demonstrated that inducing face-shear deformation is the best way to excite  $SH_0$  wave by both experiments and simulations. Undoubtedly, important progress has been made in single  $SH_0$  mode generation by face-shear piezoelectric transducers. However, there is lack of a theoretical model describing the wave field generated by the face-shear transducer. Although recently a line source mode[39, 40] for magnetostrictive EMAT and an analytical model[41] for  $SH_0$  wave generated by thickness-shear  $d_{15}$  PZT wafer are sequentially proposed, they cannot be used to solve the wavefield excited by the face-shear transducer. Currently, it is difficult for designers to control the radiation pattern of  $SH_0$  wave by optimizing the transducer's parameters (such as transducer geometry, dimensions, excitation frequency, etc.).

The motivation of the present work is to develop a theoretical model for designers to control the wave field generated by the face-shear piezoelectric transducers. In the following sections, firstly a generic procedure based on reciprocity is proposed to solve the  $SH_0$  wave field generated by arbitrary-shaped face-shear transducers bonded on an infinite isotropic plate. The model is then used to get analytical solutions for two commonly-used face-shear piezoelectric transducers: one is a single square face-shear ( $d_{24}$ ) PZT wafer, the other is a bidirectional  $SH_0$  wave transducer based on dual rectangular face-shear ( $d_{24}$ ) PZT wafers. After that, analytical solutions for the two particular transducers are verified by both finite element method (FEM) simulations and experiments. Finally, these solutions are used to optimize the transducer dimensions and a bidirectional  $SH_0$  wave piezoelectric transducer with small beam divergence angle is proposed.

## 2. $SH_0$ wave field generated by an arbitrary-shaped face-shear transducer

Consider an infinitely large isotropic plate with a thickness of  $h$ , as shown in Fig. 1(a). The

coordinate system is located at the middle plane of the plate and its 3-axis is perpendicular to the plate surface. The arbitrary-shaped face-shear transducer is surface-bonded on the plate. Several assumptions are made to establish the analytical model. Firstly, the dynamics of the transducer are ignored and the plate dynamics are assumed to be uncoupled from the transducer. This assumption was first proposed by Crawley and Luis[42] and commonly used in piezoelectric transducer modeling[43]. Secondly, the transducer and plate are assumed to be perfectly bonded, which means that transducer's strain is totally transferred to the substrate. Moreover, it is assumed that only in-plane shear strain  $\varepsilon_{12}^{\text{const}} e^{-i\omega t}$  is generated in the plate by the face-shear transducer and its magnitude is homogeneous within the bonding region  $\Omega$  shown in Fig. 1 and also uniform across the plate thickness. Based on these assumptions, the problem of solving wavefield from face-shear transducer can be regarded as an inclusion problem under a plane stress condition. Namely, a region  $\Omega$  in an infinite isotropic plate is subjected to an eigenstrain  $\varepsilon_{12}^{\text{const}} e^{-i\omega t}$ . The problem is to find the far-field particle displacements in the plate caused by the eigenstrain  $\varepsilon_{12}^{\text{const}} e^{-i\omega t}$ , which can be solved with the help of the reciprocal theorem of elastodynamics.

As shown in Fig. 1(b), let  $u_{\beta}(\mathbf{y}; \mathbf{x}) e^{-i\omega t}$  denote the  $\beta$  ( $\beta=1,2$ ) component of the displacement vector at point  $\mathbf{y}$  caused by the shear strain  $\varepsilon_{12}^{\text{const}} e^{-i\omega t}$  at point  $\mathbf{x}$  in the region  $\Omega$ . Apply a unit harmonic force  $F_{\beta}(\mathbf{y}) = 1 \cdot e^{-i\omega t}$  along  $\beta$  direction to point  $\mathbf{y}$ . According to the reciprocal theorem, we can obtain

$$1 \cdot u_{\beta}(\mathbf{y}; \mathbf{x}) = \varepsilon_{12}^{\text{const}} \sigma_{12;\beta}(\mathbf{x}; \mathbf{y}), \quad (1)$$

where  $\sigma_{12;\beta}(\mathbf{x}; \mathbf{y})$  is the shear stress at point  $\mathbf{x}$  caused by the harmonic force  $F_{\beta}(\mathbf{y})$  at point  $\mathbf{y}$ . Note that the term  $e^{-i\omega t}$  is omitted in Eq. (1) and it will be also dropped from all subsequent equations. Based on the Huygens' principle, the total displacement  $u_{\beta}(\mathbf{y})$  at point  $\mathbf{y}$  due to the eigenstrain  $\varepsilon_{12}^{\text{const}}$  in the region  $\Omega$  can be calculated by considering the region  $\Omega$  as a series of elements, each of which can be modelled as a point source. Hence, by integrating the displacement  $u_{\beta}(\mathbf{y}; \mathbf{x})$  from all the elements, the total displacement  $u_{\beta}(\mathbf{y})$  can be obtained as

$$u_\beta(\mathbf{y}) = \int_{\Omega} u_\beta(\mathbf{y}; \mathbf{x}) d\mathbf{x}_1 d\mathbf{x}_2 = \int_{\Omega} \varepsilon_{12}^{\text{const}} \sigma_{12;\beta}(\mathbf{x}; \mathbf{y}) d\mathbf{x}_1 d\mathbf{x}_2. \quad (2)$$

Using Hooke's law and the definition of strain, we have

$$\sigma_{12;\beta}(\mathbf{x}; \mathbf{y}) = \mu \left( \frac{\partial}{\partial x_2} G_{1\beta} + \frac{\partial}{\partial x_1} G_{2\beta} \right), \quad (3)$$

where  $\mu$  is the shear modulus of the isotropic plate and  $G_{\alpha\beta}(\mathbf{x}; \mathbf{y})$  denotes the  $\alpha$  ( $\alpha=1,2$ ) component of the particle displacement at point  $\mathbf{x}$  caused by the harmonic force  $F_\beta(\mathbf{y})$  at point  $\mathbf{y}$ . The Green function  $G_{\alpha\beta}(\mathbf{x}; \mathbf{y})$  for a point harmonic source located at point  $\mathbf{y}$  is given by[44]

$$G_{\alpha\beta}(\mathbf{x}; \mathbf{y}) = \frac{i}{4\mu} \left\{ \frac{1}{k_2^2} \frac{\partial}{\partial y_\alpha} \frac{\partial}{\partial y_\beta} \left[ H_0^{(1)}(k_2 r) - H_0^{(1)}(k_1 r) \right] + \delta_{\alpha\beta} H_0^{(1)}(k_2 r) \right\}, \quad (4)$$

where  $r$  is defined by

$$r = \sqrt{(x_1 - y_1)^2 + (x_2 - y_2)^2}. \quad (5)$$

The term  $H_0^{(1)}(\cdot)$  is the Hankel function of the first kind of order zero and the term  $k_\alpha$  denotes the wavenumber given by

$$k_\alpha = \frac{\omega}{c_\alpha}, \quad \alpha=1,2, \quad c_1 = \sqrt{\frac{\lambda_{Lame} + 2\mu}{\rho}} \quad \text{and} \quad c_2 = \sqrt{\frac{\mu}{\rho}}, \quad (6)$$

where  $\lambda_{Lame}$  is Lamé constant and  $\rho$  is the density of the plate. Using Eqs. (2) and (3), one can show that

$$u_\beta(\mathbf{y}) = \mu \varepsilon_{12}^{\text{const}} \int_{\Omega} \left[ \frac{\partial}{\partial x_2} G_{1\beta}(\mathbf{x}; \mathbf{y}) + \frac{\partial}{\partial x_1} G_{2\beta}(\mathbf{x}; \mathbf{y}) \right] d\mathbf{x}_1 d\mathbf{x}_2. \quad (7)$$

Using Green's formula, Eq. (7) can be expressed in a line integral form as

$$u_\beta(\mathbf{y}) = \mu \varepsilon_{12}^{\text{const}} \oint_C \left[ -G_{1\beta}(\mathbf{x}; \mathbf{y}) d\mathbf{x}_1 + G_{2\beta}(\mathbf{x}; \mathbf{y}) d\mathbf{x}_2 \right], \quad (8)$$

where  $C$  is a positively oriented, smooth and closed curve, which bounds the region  $\Omega$ . It should be noted that the conversion from surface integral to line integral has a clear physical meaning, which will be discussed in detail in Section 3.

Because the particle displacement of the  $\text{SH}_0$  wave is in-plane and perpendicular to its propagating direction, we need to calculate the tangential displacement  $u_\theta$  in the polar coordinate system. As shown in Fig. 1(b),  $u_\theta$  can be obtained from the displacement component

$u_\beta(\mathbf{y})$  in the Cartesian coordinate system:

$$u_\theta(r_0, \theta) = -u_1 \sin \theta + u_2 \cos \theta. \quad (9)$$

Next, based on Eq. (8), Eq. (9) can be rewritten as:

$$u_\theta(r_0, \theta) = \mu \varepsilon_{12}^{\text{const}} \left\{ \begin{aligned} & - \left\{ \oint_C [-G_{11}(\mathbf{x}; \mathbf{y})] dx_1 + G_{21}(\mathbf{x}; \mathbf{y}) dx_2 \right\} \sin \theta \\ & + \left\{ \oint_C [-G_{12}(\mathbf{x}; \mathbf{y})] dx_1 + G_{22}(\mathbf{x}; \mathbf{y}) dx_2 \right\} \cos \theta \end{aligned} \right\}. \quad (10)$$

Similarly, we can also calculate the radial displacement  $u_r$  in the polar coordinate system:

$$u_r(r_0, \theta) = \mu \varepsilon_{12}^{\text{const}} \left\{ \begin{aligned} & \left\{ \oint_C [-G_{11}(\mathbf{x}; \mathbf{y})] dx_1 + G_{21}(\mathbf{x}; \mathbf{y}) dx_2 \right\} \cos \theta \\ & + \left\{ \oint_C [-G_{12}(\mathbf{x}; \mathbf{y})] dx_1 + G_{22}(\mathbf{x}; \mathbf{y}) dx_2 \right\} \sin \theta \end{aligned} \right\}. \quad (11)$$

Actually, Eq. (9) can further be simplified as follows. Put

$$I(a, b) = \mu \varepsilon_{12}^{\text{const}} \left\{ \begin{aligned} & - \left\{ \int_a^b [-G_{11}(\mathbf{x}; \mathbf{y})] dx_1 + G_{21}(\mathbf{x}; \mathbf{y}) dx_2 \right\} \sin \theta \\ & + \left\{ \int_a^b [-G_{12}(\mathbf{x}; \mathbf{y})] dx_1 + G_{22}(\mathbf{x}; \mathbf{y}) dx_2 \right\} \cos \theta \end{aligned} \right\}, \quad (12)$$

where  $a$  and  $b$  are arbitrary constants related to the closed curve  $C$ . Obviously,  $u_\theta(r_0, \theta)$  is the superposition of a series of  $I(a, b)$ . Combining Eqs. (4) and (12), the universal term

$\int_a^b G_{\alpha\beta}(\mathbf{x}; \mathbf{y}) dx_\alpha$  in Eq. (12) is given by

$$\begin{aligned} \int_a^b G_{\alpha\beta}(\mathbf{x}; \mathbf{y}) dx_\alpha &= \int_a^b \frac{i}{4\mu} \left\{ -\frac{1}{k_2^2} \frac{\partial}{\partial x_\alpha} \frac{\partial}{\partial y_\beta} [H_0^{(1)}(k_2 r) - H_0^{(1)}(k_1 r)] + \delta_{\alpha\beta} H_0^{(1)}(k_2 r) \right\} dx_\alpha \\ &= \frac{i}{4\mu} \left\{ -\frac{1}{k_2^2} \frac{\partial}{\partial y_\beta} [H_0^{(1)}(k_2 r) - H_0^{(1)}(k_1 r)] \right\}_{x_\alpha=a}^{x_\alpha=b} + \int_a^b \delta_{\alpha\beta} H_0^{(1)}(k_2 r) dx_\alpha \\ &= \frac{i}{4\mu} \left\{ -\frac{(x_\beta - y_\beta)}{k_2^2 r} [k_2 H_1^{(1)}(k_2 r) - k_1 H_1^{(1)}(k_1 r)] \right\}_{x_\alpha=a}^{x_\alpha=b} + \int_a^b \delta_{\alpha\beta} H_0^{(1)}(k_2 r) dx_\alpha \end{aligned} \quad (13)$$

Using the far-field approximation ( $r \gg R$  shown in Fig. 1(b)), we have

$$\begin{aligned} y_1 - x_1 &\approx r \cos \theta \\ y_2 - x_2 &\approx r \sin \theta. \end{aligned} \quad (14)$$

Then using Eqs. (12), (13) and (14), we get

$$I(a, b) = \frac{i \varepsilon_{12}^{\text{const}}}{4} \left[ \sin \theta \int_a^b H_0^{(1)}(k_2 r) dx_1 + \cos \theta \int_a^b H_0^{(1)}(k_2 r) dx_2 \right]. \quad (15)$$

Thus, Eq. (10) becomes

$$u_\theta(r_0, \theta) = \frac{i \varepsilon_{12}^{\text{const}}}{4} \left[ \sin \theta \oint_C H_0^{(1)}(k_2 r) dx_1 + \cos \theta \oint_C H_0^{(1)}(k_2 r) dx_2 \right]. \quad (16)$$

Eq. (16) implies that the SH<sub>0</sub> wave field is only determined by the third term  $\delta_{\alpha\beta} H_0^{(1)}(k_2 r)$  in the

Green function  $G_{\alpha\beta}(\mathbf{x};\mathbf{y})$ .

It should be noted that only the  $SH_0$  wave strictly satisfies the plane stress condition, so the proposed model can, strictly speaking, only be used to describe  $SH_0$  wave field. However, because the in-plane radial displacement of the  $S_0$  mode (the fundamental symmetric Lamb wave mode) in a plate is dominant and almost constant across the thickness of the plate at low frequency-thickness product values, the radial displacement  $u_r$  given by Eq. (11) can also be used to roughly describe the  $S_0$  wave in plates.

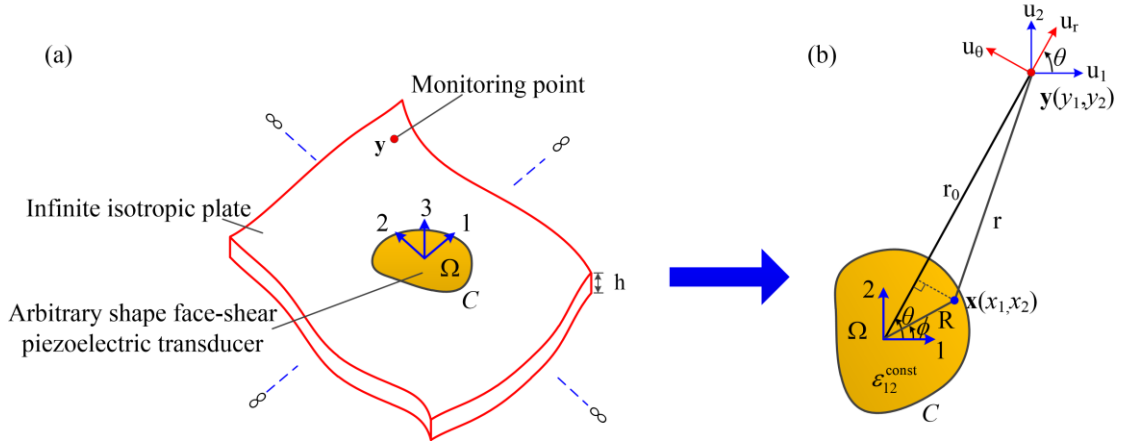


**Fig 1.** (a) Arbitrary-shaped face-shear piezoelectric transducer bonded on the surface of an infinite large plate, (b) the coordinate systems used in theoretical analysis.

### 3. Particular face-shear $SH_0$ wave transducer configurations

In this section, we will use the general derivation from Section 2 to solve the  $SH_0$  wave field generated by two commonly-used face-shear  $SH_0$  wave transducers: one is a single square face-shear ( $d_{24}$ ) PZT wafer[36], the other is a bidirectional  $SH_0$  wave piezoelectric transducer (BSH-PT) based on dual rectangular face-shear ( $d_{24}$ ) PZT wafers[16].

#### 3.1 Square face-shear PZT wafer

Fig. 2(a) shows a schematic for a square face-shear PZT wafer bonded on the surface of an infinitely large plate. The length of the square wafer is set to be  $2L$  and the coordinate system used for theoretical analysis is illustrated in Fig. 2(b). In this case, Eq. (8) can be rewritten as

$$u_{\beta}(\mathbf{y}) = \mu \varepsilon_{12}^{\text{const}} \left\{ - \int_{x_1=-L}^{x_1=+L} [G_{1\beta}(\mathbf{x};\mathbf{y})]_{x_2=-L} dx_1 + \int_{x_1=-L}^{x_1=+L} [G_{1\beta}(\mathbf{x};\mathbf{y})]_{x_2=+L} dx_1 \right. \\ \left. + \int_{x_2=-L}^{x_2=+L} [G_{2\beta}(\mathbf{x};\mathbf{y})]_{x_1=+L} dx_2 - \int_{x_2=-L}^{x_2=+L} [G_{2\beta}(\mathbf{x};\mathbf{y})]_{x_1=-L} dx_2 \right\}. \quad (17)$$

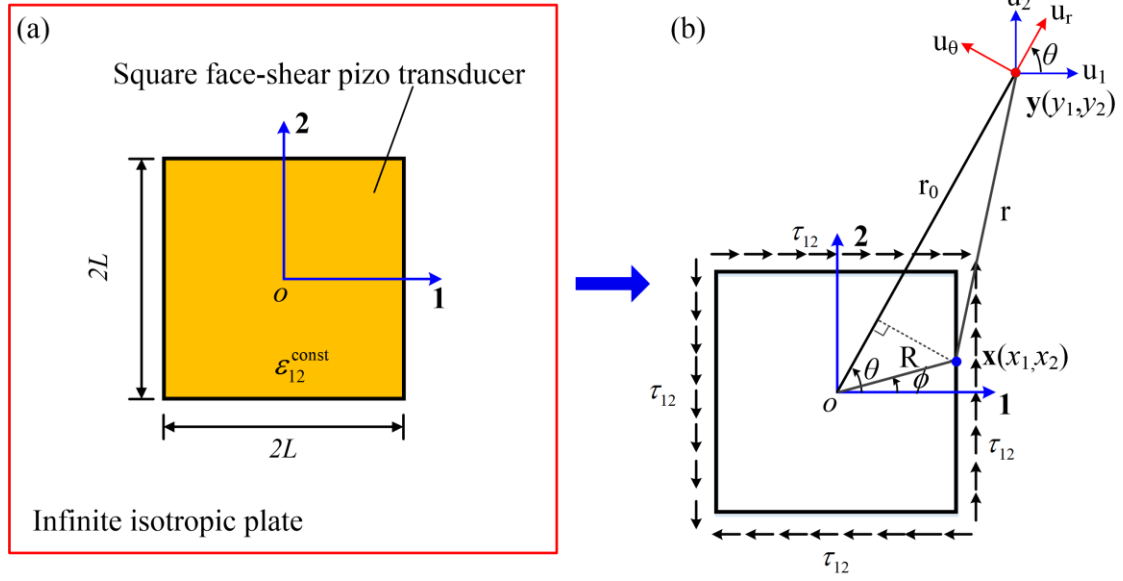


**Fig. 2** Schematic of the physical meaning of the proposed model for a square face-shear transducer. Namely, the wave field generated by a face-shear transducer is equivalent to that generated by uniform in-plane tractions along its perimeter.

It should be noted, from Eq. (13), that the value of  $\int_a^b G_{\alpha\beta}(\mathbf{x};\mathbf{y})d\mathbf{x}_\alpha$  is the same when the term  $G_{\alpha\beta}(\mathbf{x};\mathbf{y})$  is replaced by  $G_{\beta\alpha}(\mathbf{y};\mathbf{x})$ , where  $G_{\beta\alpha}(\mathbf{y};\mathbf{x})$  denotes the  $\beta$  ( $\beta=1,2$ ) component of the particle displacement at point  $\mathbf{y}$  caused by the harmonic force  $F_\alpha(\mathbf{x})$  at point  $\mathbf{x}$ . Hence, the term  $G_{\alpha\beta}(\mathbf{x};\mathbf{y})$  can also denote the  $\beta$  component of the particle displacement at point  $\mathbf{y}$  caused by the harmonic force  $F_\alpha(\mathbf{x})$  at point  $\mathbf{x}$ . Therefore, the physical meaning of the term  $-\mu\epsilon_{12}^{\text{const}} \int_{x_1=-L}^{x_1=+L} [G_{1\beta}(\mathbf{x};\mathbf{y})]_{x_2=-L} d\mathbf{x}_1$  in Eq. (17) can be understood as follow: there are uniform in-plane tractions (say  $\mu\epsilon_{12}^{\text{const}}$  per unit length) along the perimeter line  $x_2 = -L$  in the negative 1-axis direction as shown in Fig. 2(b) and the wave field caused by the in-plane tractions is given by  $-\mu\epsilon_{12}^{\text{const}} \int_{x_1=-L}^{x_1=+L} [G_{1\beta}(\mathbf{x};\mathbf{y})]_{x_2=-L} d\mathbf{x}_1$ . The direction of the line integral is opposite to that of in-plane tractions, so there is a negative sign in the term  $-\mu\epsilon_{12}^{\text{const}} \int_{x_1=-L}^{x_1=+L} [G_{1\beta}(\mathbf{x};\mathbf{y})]_{x_2=-L} d\mathbf{x}_1$ . Similarly, based on the physical meaning of other three terms in Eq. (17), we can draw all the in-plane tractions on the perimeter of the face-shear transducer, as shown in Fig. 2(b). Therefore, Eq. (17) indicates that the wave field generated by a face-shear transducer is equivalent to that

generated by uniform in-plane tractions along its perimeter, as shown in Fig. 2. It is not difficult to infer that this physical meaning is also valid for the general Eq. (8).

Now, we calculate the  $SH_0$  wave field generated by a square face-shear transducer. Eq. (16) for this case can be rewritten as

$$u_\theta(r_0, \theta) = \frac{i\varepsilon_{12}^{\text{const}}}{4} \left\{ - \left\{ - \int_{x_1=-L}^{x_1=+L} \left[ H_0^{(1)}(k_2 r) \right]_{x_2=-L} dx_1 + \int_{x_1=-L}^{x_1=+L} \left[ H_0^{(1)}(k_2 r) \right]_{x_2=+L} dx_1 \right\} \sin \theta \right. \\ \left. + \left\{ + \int_{x_2=-L}^{x_2=+L} \left[ H_0^{(1)}(k_2 r) \right]_{x_1=+L} dx_2 - \int_{x_2=-L}^{x_2=+L} \left[ H_0^{(1)}(k_2 r) \right]_{x_1=-L} dx_2 \right\} \cos \theta \right\}. \quad (18)$$

In order to get the analytical solutions, the asymptotic expression of the Hankel function  $H_0^{(1)}(k_2 r)$  is used for the far field case:

$$\lim_{k_2 r \rightarrow \infty} H_0^{(1)}(k_2 r) = \sqrt{\frac{2}{\pi k_2 r}} e^{i \left( k_2 r - \frac{\pi}{4} \right)}. \quad (19)$$

In practice, when the measurement point is four or five spatial wavelengths away from the wave source, the Hankel function and its asymptotic expression are pretty close. Moreover, using the far-field approximation ( $r \gg R$  shown in Fig. 2(b)), we also have:

$$\begin{aligned} r &= r_0 - R \cos(\theta - \varphi) \\ &= r_0 - R(\cos \theta \cos \varphi + \sin \theta \sin \varphi). \\ &= r_0 - x_1 \cos \theta - x_2 \sin \theta \end{aligned} \quad (20)$$

Substituting Eq. (20) into Eq. (19) yields

$$H_0^{(1)}(k_2 r) \approx \sqrt{\frac{2}{\pi k_2 r_0}} \exp \left[ i \left( k_2 r_0 - \frac{\pi}{4} \right) \right] \exp \left[ -i k_2 (x_1 \cos \theta + x_2 \sin \theta) \right]. \quad (21)$$

Then by substituting Eq. (21) into Eq. (18), the analytical solution for the  $SH_0$  wave field generated by a square face-shear transducer is obtained as

$$u_\theta(r_0, \theta) = 2\varepsilon_{12}^{\text{const}} L \sqrt{\frac{2}{\pi k_2 r_0}} \frac{\sin(k_2 L \sin \theta) [\sin(k_2 L \cos \theta)] \cos 2\theta}{k_2 L \sin 2\theta} \exp \left[ i \left( k_2 r_0 - \frac{\pi}{4} \right) \right]. \quad (22)$$

Similarly, expressions for the radial displacement can be obtained as follows. Eq. (11) for the square transducer can be rewritten as

$$u_r(r_0, \theta) = \mu \varepsilon_{12}^{\text{const}} \left\{ \begin{aligned} & \left\{ -\int_{x_1=-L}^{x_1=+L} [G_{11}(\mathbf{x}; \mathbf{y})]_{x_2=-L} dx_1 + \int_{x_1=-L}^{x_1=+L} [G_{11}(\mathbf{x}; \mathbf{y})]_{x_2=+L} dx_1 \right. \\ & \left. + \left\{ +\int_{x_2=-L}^{x_2=+L} [G_{21}(\mathbf{x}; \mathbf{y})]_{x_1=+L} dx_2 - \int_{x_2=-L}^{x_2=+L} [G_{21}(\mathbf{x}; \mathbf{y})]_{x_1=-L} dx_2 \right\} \right\} \cos \theta \\ & + \left\{ -\int_{x_1=-L}^{x_1=+L} [G_{12}(\mathbf{x}; \mathbf{y})]_{x_2=-L} dx_1 + \int_{x_1=-L}^{x_1=+L} [G_{12}(\mathbf{x}; \mathbf{y})]_{x_2=+L} dx_1 \right. \\ & \left. + \left\{ +\int_{x_2=-L}^{x_2=+L} [G_{22}(\mathbf{x}; \mathbf{y})]_{x_1=+L} dx_2 - \int_{x_2=-L}^{x_2=+L} [G_{22}(\mathbf{x}; \mathbf{y})]_{x_1=-L} dx_2 \right\} \right\} \sin \theta \end{aligned} \right\}. \quad (23)$$

When the far-field approximation is used, the asymptotic expression of the Hankel function

$H_1^{(1)}(k_\alpha r)$  ( $\alpha=1,2$ ) is given by

$$H_1^{(1)}(k_\alpha r) \approx \sqrt{\frac{2}{\pi k_\alpha r_0}} \exp\left[i\left(k_\alpha r_0 - \frac{3\pi}{4}\right)\right] \exp[-ik_\alpha (x_1 \cos \theta + x_2 \sin \theta)]. \quad (24)$$

Using Eqs. (13), (21), (23) and (24), we have

$$u_r(r_0, \theta) = \frac{2k_1}{k_2^2} \varepsilon_{12}^{\text{const}} \sqrt{\frac{2}{\pi k_1 r_0}} [\sin(k_1 L \sin \theta) \sin(k_1 L \cos \theta)] \exp\left[i\left(k_1 r_0 - \frac{\pi}{4}\right)\right]. \quad (25)$$

This analytical expression can be used to roughly describe the  $S_0$  wave field caused by a square face-shear transducer.

### 3.2 Bidirectional $SH_0$ wave piezoelectric transducer

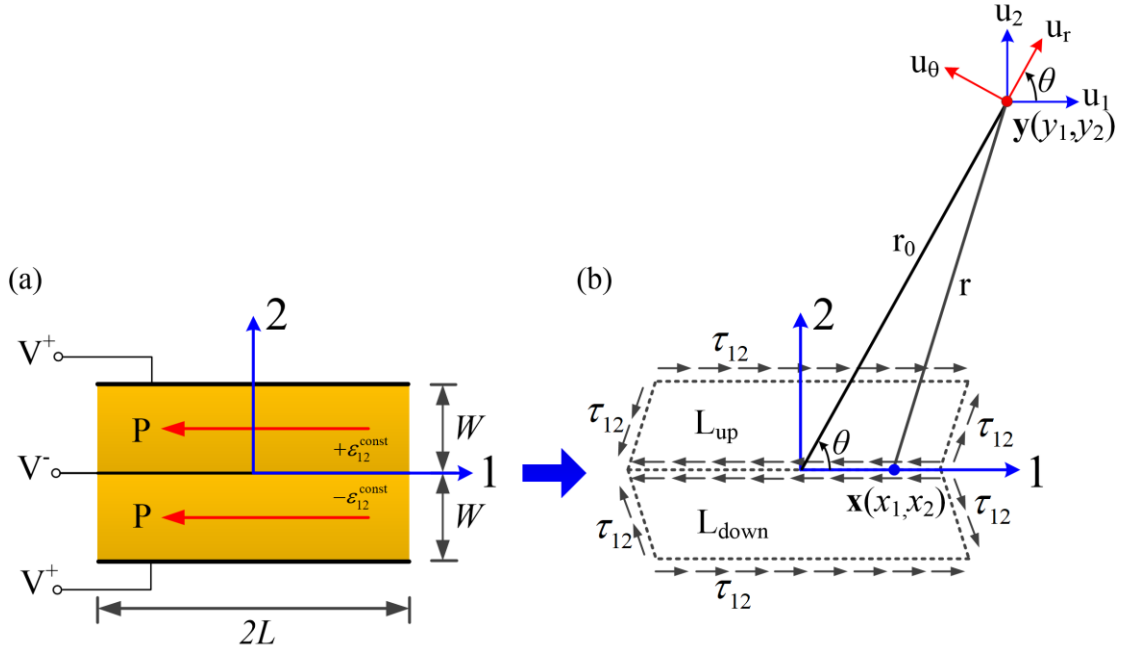


**Fig. 3** (a) Schematics of the bidirectional  $SH_0$  wave piezoelectric transducer, (b) the coordinate system and effective shear tractions used in theoretical analysis.

The bidirectional  $SH_0$  wave piezoelectric transducer (BSH-PT) was proposed by Miao et al.[16]. As shown in Fig. 3(a), the BSH-PT is made up of two identical rectangular face-shear ( $d_{24}$ ) PZT wafers. The length of the PZT wafer is set to be  $2L$  and its width is  $W$ . The coordinate system used for theoretical analysis is illustrated in Fig. 3(b). When an electric field is applied to the BSH-PT, the face-shear deformations of the two PZT wafers are opposite due to their opposite drive field. Such an opposite face-shear deformation makes the BSH-PT capable of exciting pure  $SH_0$  wave and focusing the wave energy along two opposite directions ( $90^\circ$  and  $270^\circ$ ) over a wide frequency range. Based on Huygens' principle, the wave field caused by the BSH-PT can be modeled as the superposition of the fields generated by each individual rectangular PZT wafer. Moreover, Eq. (8) indicates that the partial wave filed caused by the rectangular face-shear PZT wafer is equivalent to that generated by uniform in-plane tractions along the wafer's perimeter. Therefore, by integrating the displacement caused by the tractions shown in Fig. 3(b), we can obtain the wave field caused by the BSH-PT. Based on Eq. (16), the tangential displacement caused by the BSH-PT is given by

$$u_\theta(r_0, \theta) = \frac{i\mathcal{E}_{12}^{\text{const}}}{4} \left[ \sin \theta \oint_{L_{\text{up}}} H_0^{(1)}(k_2 r) dx_1 + \cos \theta \oint_{L_{\text{up}}} H_0^{(1)}(k_2 r) dx_2 \right] - \frac{i\mathcal{E}_{12}^{\text{const}}}{4} \left[ \sin \theta \oint_{L_{\text{down}}} H_0^{(1)}(k_2 r) dx_1 + \cos \theta \oint_{L_{\text{down}}} H_0^{(1)}(k_2 r) dx_2 \right]. \quad (26)$$

Substituting Eq. (21) into Eq. (26), we can get the analytical expression for the  $SH_0$  wave filed as follows

$$u_\theta(r_0, \theta) = \frac{2i\mathcal{E}_{12}^{\text{const}}}{k_2} \sqrt{\frac{2}{\pi k_2 r_0}} \frac{[1 - \cos(k_2 W \sin \theta)] \sin(k_2 L \cos \theta) \cos 2\theta}{\sin 2\theta} \exp \left[ i \left( k_2 r_0 - \frac{\pi}{4} \right) \right]. \quad (27)$$

Similarly, based on Eq. (11), we can calculate the radial displacement caused by the BSH-PT as follows

$$\frac{u_r(r_0, \theta)}{\mu \mathcal{E}_{12}^{\text{const}}} = \left\{ \oint_{L_{\text{up}}} [-G_{11}(\mathbf{x}; \mathbf{y})] dx_1 + G_{21}(\mathbf{x}; \mathbf{y}) dx_2 - \oint_{L_{\text{down}}} [-G_{11}(\mathbf{x}; \mathbf{y})] dx_1 + G_{21}(\mathbf{x}; \mathbf{y}) dx_2 \right\} \cos \theta + \left\{ \oint_{L_{\text{up}}} [-G_{12}(\mathbf{x}; \mathbf{y})] dx_1 + G_{22}(\mathbf{x}; \mathbf{y}) dx_2 + \oint_{L_{\text{down}}} [-G_{12}(\mathbf{x}; \mathbf{y})] dx_1 + G_{22}(\mathbf{x}; \mathbf{y}) dx_2 \right\} \sin \theta \quad (28)$$

Using Eqs. (13), (21) and (24), Eq. (28) is simplified to be

$$u_r(r_0, \theta) = \frac{2ik_1}{k_2^2} \mathcal{E}_{12}^{\text{const}} \sqrt{\frac{2}{\pi k_1 r_0}} [1 - \cos(k_1 W \sin \theta)] \sin(k_1 L \cos \theta) \exp \left[ i \left( k_1 r_0 - \frac{\pi}{4} \right) \right]. \quad (29)$$

#### 4. Verification of theoretical analysis by simulations and experiments

In this Section, finite element method (FEM) simulations and experiments are performed to verify the analytical expressions obtained in Section 3. The FEM simulations are conducted using ANSYS software. The square face-shear transducer in the simulation is made up of a  $d_{24}$  PZT-5H wafer with the dimensions of  $6\text{ mm} \times 6\text{ mm} \times 1\text{ mm}$ . The detailed information on the square face-shear  $d_{24}$  PZT wafer can be found in reference[36]. The bidirectional  $SH_0$  wave piezoelectric transducer used in the simulation consists of two rectangular  $d_{24}$  PZT-5H elements with the dimensions of  $24.8\text{ mm} \times 6.2\text{ mm} \times 1\text{ mm}$ . The detailed information on the bidirectional  $SH_0$  wave piezoelectric transducer and the material parameters of the PZT-5H ceramics can be found in reference[16]. An aluminum plate with the dimensions of  $400\text{ mm} \times 400\text{ mm} \times 1\text{ mm}$  is used as the waveguide in simulations. The Young's modulus, Poisson ratio and density of the aluminum plate are 69 GPa, 0.33 and  $2700\text{ kg/m}^3$ , respectively. Transducers for all cases are placed at the center of the aluminum plate and all the excited wave fields are extracted at a short distance from the center of the transducer. The SOLID5 element in the ANSYS software is used to model PZT wafers and the aluminum plate is modeled by SOLID185 elements. In order to ensure the accuracy of the computational results, the mesh density and time step are set as follows: the largest size of elements is less than  $1/20$  of the shortest wavelength and the time step is less than  $1/(20f_c)$ , where  $f_c$  is the central frequency of the drive signal.

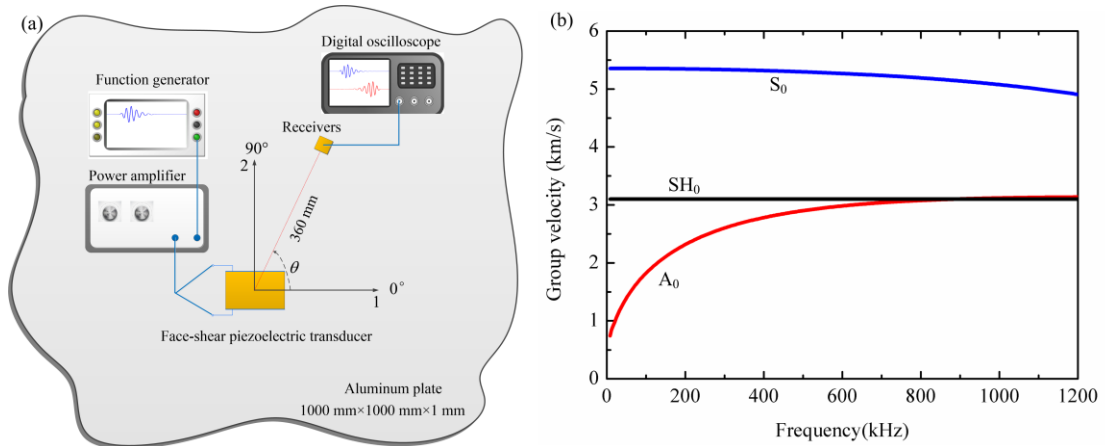


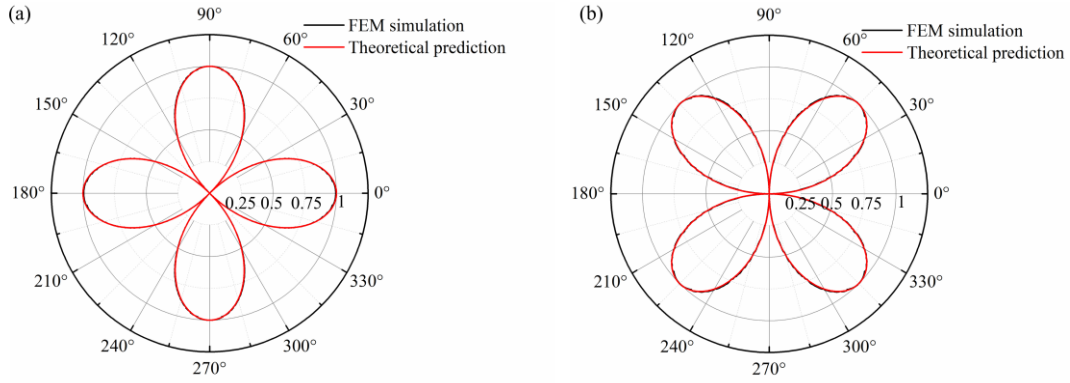
**Fig. 4** (a) Schematic of the experimental setup for measuring the wave field of face-shear piezoelectric transducers. (b) Group velocity dispersion curve of the  $SH_0$  wave and Lamb waves in a 1 mm thick aluminum plate.

Experimental setup for measuring the wave field generated by face-shear transducers is illustrated in Fig. 4(a). Transducers used in experiments have the same size and material parameters as that used in the finite element simulations. For all cases, transducers are bonded on the center of the aluminum plate ( $1000\text{ mm} \times 1000\text{ mm} \times 1\text{ mm}$ ) using epoxy resin and driven by a five-cycle Hanning window-modulated sinusoid toneburst signal. The drive signal was provided by a function generator (DG4062, Rigol, China) and amplified by a power amplifier (KH7602M). A face-shear  $d_{36}$  PMN-PT single crystal wafer ( $d_{36}=1600\text{ pC/N}$  and  $d_{31}=-360\text{ pC/N}$ ,  $5\text{ mm} \times 5\text{ mm} \times 1\text{ mm}$ ) was used as a sensor to measure the wave field generated by the square face-shear  $d_{24}$  PZT wafer, since it can detect both  $SH_0$  wave and Lamb waves[32]. As our previous study[16] showed that almost no Lamb waves were generated by the bidirectional  $SH_0$  wave piezoelectric transducer (BSH-PT), face-shear  $d_{24}$  PZT wafers ( $6\text{ mm} \times 6\text{ mm} \times 1\text{ mm}$ ) were used as sensors to measure the  $SH_0$  wave field caused by the BSH-PT. As shown in Fig. 4(a), the orientation of the sensor is along the red dotted line connecting the transducer and the sensor, and the distance between them is fixed at 360 mm. The signal measured by sensors was collected by an oscilloscope (Tektronix TBS2014) with 128 times trace averaging. The  $SH_0$ ,  $S_0$  and  $A_0$  wave modes in the received signals are identified based on their different group velocities and their dispersion curves in the 1mm thick aluminum plate are illustrated in Fig. 4(b).

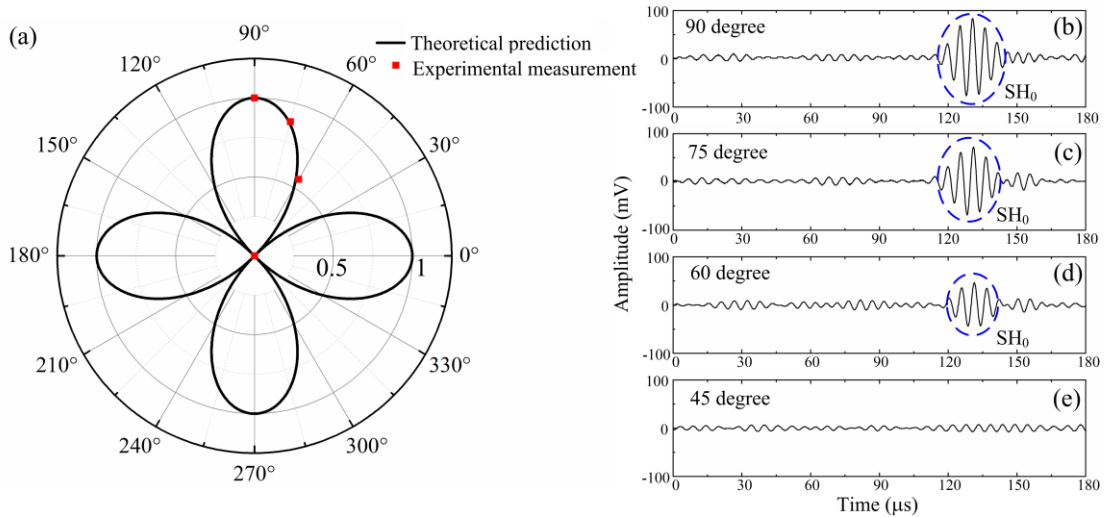
#### 4.1 Square face-shear PZT wafer

Fig. 5 shows the FEM simulated displacement wavefields in an aluminum plate excited by a square face-shear ( $d_{24}$ ) PZT wafer at 165 kHz. The theoretical predictions by Eq. (22) and Eq. (25) are also plotted in Fig. 5 for comparison. Note that both the tangential and radial displacements are normalized against the maximum amplitude of each case. It can be seen that the theoretical predictions are in perfect agreement with the finite element simulations for both the  $SH_0$  wave and the  $S_0$  wave, which confirms the validity of the proposed theoretical model. Fig. 5 shows that the amplitude of the excited  $SH_0$  wave reaches its maximum value at  $0^\circ$ ,  $90^\circ$ ,  $180^\circ$  and  $270^\circ$  directions, while the maximum amplitude of the  $S_0$  mode occurs at  $45^\circ$ ,  $135^\circ$ ,  $225^\circ$  and  $315^\circ$  directions. It is not difficult to understand this phenomenon because the strain field is a tensor field. The  $45^\circ$  (or  $225^\circ$ ) and  $135^\circ$  (or  $315^\circ$ ) directions are the principal directions of a pure face-shear strain state. Only normal strain components (elongation or contraction) are non-zero relative to principal

directions, so Lamb waves are generated at the principal directions. As we know, the magnetostrictive EMATs can generate  $SH_0$  wave also by inducing face-shear deformation based on the so-called “Wiedemann effect”[23], i.e., when a large dc magnetic field is applied to a magnetostrictive material in one in-plane direction and an ac magnetic field is applied in another orthogonal in-plane direction, face-shear deformation will be produced in the material. Therefore, the analytical solutions given by Eq. (22) and Eq. (25) are also valid for the similar configuration magnetostrictive EMATs.



**Fig. 5** Comparison of the FEM simulated and theoretically predicted wave fields in an aluminum plate generated by a square face-shear ( $d_{24}$ ) PZT wafer at 165 kHz: (a) tangential displacement ( $SH_0$  wave) and (b) radial displacement ( $S_0$  wave). The plots are normalized against the maximum amplitude of each case.



**Fig. 6** (a) Comparison of experimentally measured and theoretically predicted  $SH_0$  wave field in an aluminum plate generated by a square face-shear ( $d_{24}$ ) PZT wafer at 165 kHz. (b-e) Wave signals measured by the  $d_{36}$  PMN-PT wafer at different directions.

Fig. 6(b-e) present the  $SH_0$  wave signals generated by a square face-shear ( $d_{24}$ ) PZT wafer under a voltage of 40 V and measured by a  $d_{36}$  PMN-PT wafer at different directions. The peak-to-peak amplitudes of the excited  $SH_0$  wave are then extracted and normalized against the maximum value at  $90^\circ$  direction to compare with the theoretical predictions, as shown in Fig. 6(a). Obviously, the measured wavefield accords very well with the theoretical predictions, which further validates the proposed theoretical model.

#### 4.2 Bidirectional $SH_0$ wave piezoelectric transducer

Fig. 7 presents the FEM simulated and theoretically predicted  $SH_0$  wave radiation patterns of the BSH-PT at 200 kHz. The amplitudes of the tangential displacement predicated by Eq. (27) at different radiation angle  $\theta$  are normalized against its maximum value to compare with the FEM simulated radiation pattern, which is also normalized. It can be seen from Fig. 7(a) that the analytical solution given by Eq. (27) predicts the radiation pattern very well. The main lobes of the wave beam are precisely predicated, even the prediction of side lobes is also very good. Similarly, the comparison of theoretically predicted and FEM simulated radial displacement wavefields is shown in Fig. 7(b), in which the radial displacement is normalized against the maximum amplitude of the tangential displacement. Obviously, the radial displacement wavefield predicted by Eq. (29) accords well with the simulation. It should be noted that the radial displacement is quite small compared with the maximum tangential displacement, which indicates that almost no  $S_0$  mode is generated by the BSH-PT. This phenomenon is also in good agreement with our previous experiments[16].

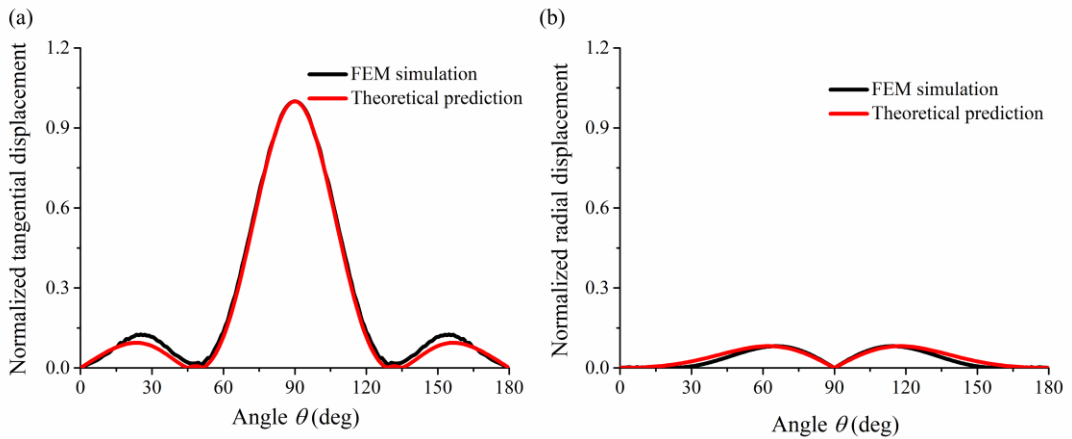


**Fig. 7** Comparison of the theoretically predicated and FEM simulated wave fields in an aluminum

plate generated by a bidirectional  $SH_0$  wave piezoelectric transducer at 200 kHz: (a) tangential displacement ( $SH_0$  wave) and (b) radial displacement ( $S_0$  wave). The plots are normalized against the maximum amplitude of the tangential displacement.

Fig. 8 presents the experimentally measured  $SH_0$  wave field excited by the BSH-PT under a voltage of 15 V. After normalizing the peak-to-peak amplitudes of the measured  $SH_0$  wave against the maximum value at  $90^\circ$  direction, we can get the radiation pattern and compare it with the theoretical predictions. It can be seen that the proposed model can well predict the radiation pattern of the BSH-PT, which further confirms the validity of the proposed analytical model.

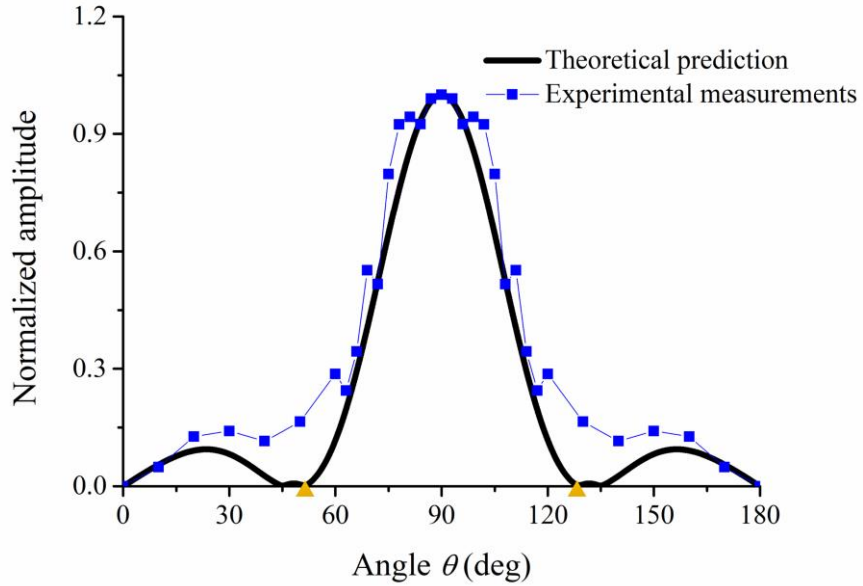


**Fig. 8** Comparison of the measured and theoretically predicated  $SH_0$  wave field in an aluminum plate generated by a bidirectional  $SH_0$  wave piezoelectric transducer at 200 kHz. The angle marked by the yellow triangle is the beam divergence angle.

## 5. Optimization of the face-shear transducers

Since the proposed analytical model has been validated by both experiments and FEM simulations, it is instructive to use it to obtain some general guidelines for the design of  $SH_0$  wave face-shear transducers. In this section, the optimal dimensions for the face-shear piezoelectric transducer to generate the desired  $SH_0$  wavefield are derived.

### 5.1 The case of a square face-shear $d_{24}$ PZT wafer

Fig. 5 has indicated that a square face-shear PZT wafer will generate pure  $SH_0$  wave along

four main directions ( $0^\circ$ ,  $90^\circ$ ,  $180^\circ$  and  $270^\circ$ ), accompanied by Lamb waves along the diagonal of the wafer. It is therefore desirable to suppress the unwanted Lamb waves by optimizing dimensions of the transducer. We can get the maximum amplitude of the excited  $SH_0$  wave from Eq. (22) as follows

$$|u_\theta(r_0, \theta)|_{\max} = |u_\theta(r_0, 0)| = \varepsilon_{12}^{\text{const}} L \sqrt{\frac{2}{\pi k_2 r_0}} |\sin(k_2 L)|. \quad (30)$$

Similarly, based on Eq. (25), the maximum amplitude of the possible  $S_0$  mode is given by

$$|u_r(r_0, \theta)|_{\max} = \left| u_r\left(r_0, \frac{\pi}{4}\right) \right| = \left| 2\varepsilon_{12}^{\text{const}} \frac{k_1}{k_2^2} \sqrt{\frac{2}{\pi k_1 r_0}} \sin^2\left(\frac{\sqrt{2}}{2} k_1 L\right) \right|. \quad (31)$$

The amplitude ratio of  $S_0$  mode to  $SH_0$  mode is then defined as

$$\kappa = \frac{|u_r(r_0, \theta)|_{\max}}{|u_\theta(r_0, \theta)|_{\max}} = \frac{2\sqrt{k_1 k_2} \sin^2\left(\frac{\sqrt{2}}{2} k_1 L\right)}{k_2^2 L \sin(k_2 L)}. \quad (32)$$

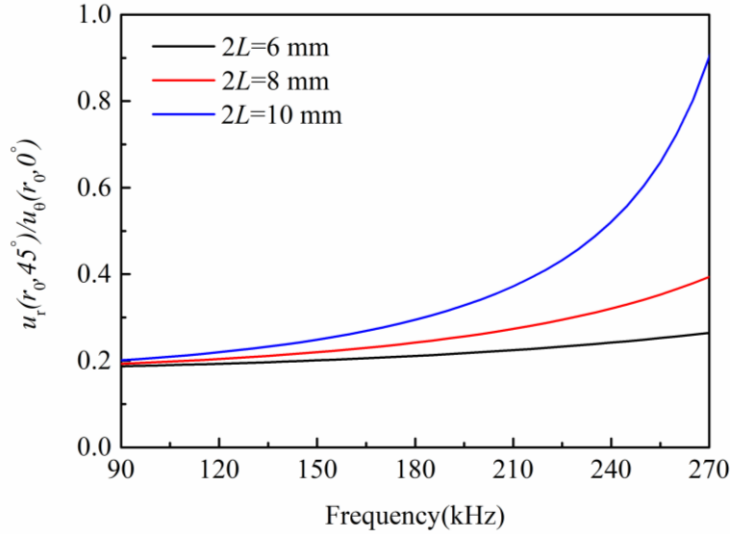


**Fig. 9** The theoretically predicted amplitude ratio of  $S_0$  mode to  $SH_0$  mode excited by the square face-shear PZT wafer with different dimensions.

Obviously, the amplitude ratio  $\kappa$  should be as small as possible for a  $SH_0$  wave transducer. Fig. 9 presents the theoretically predicted frequency dependent amplitude ratio  $\kappa$  for square face-shear PZT wafers with different dimensions bonded on a 1mm-thick, infinitely large aluminum plate. It can be seen that the amplitude ratio always increases with frequency and the

slope is strongly influenced by the transducer size. For the transducer with the side length of 6 mm, the ratio  $\kappa$  is only about 20% and almost keeps constant in the frequency range from 90 kHz to 270 kHz. This implies that the generated  $S_0$  mode is quite small and can be neglected, which accords well with the experimental result shown in Fig. 6(e). When the size of the transducer increases to 8 mm, although the ratio  $\kappa$  becomes higher especially at high frequency, no significant change is observed compared with the case of 6 mm. However, when the transducer size further increases to 10 mm, the increase rate of the ratio  $\kappa$  becomes large at high frequency, which indicates that significant  $S_0$  mode will be generated at high frequency.

The above phenomenon is then confirmed by FEM simulations. Fig. 10 presents the FEM simulated displacement time history of guided waves in a 1mm-thick aluminum plate excited by square face-shear  $d_{24}$  PZT wafers with two different sizes (8 mm $\times$ 8 mm $\times$ 1 mm and 10 mm $\times$ 10 mm $\times$ 1 mm) under a voltage of 15 V at 200 kHz, respectively. For each case, the tangential displacement time history at 0° direction and the radial displacement time history at 45° direction are extracted 40 mm away from the center of wafer and normalized against the maximum tangential displacement. As expected, Fig.10 shows that the amplitude ratio of  $S_0$  mode to  $SH_0$  mode increases with the increasing size of the wafer, which accords well with the theoretical predication shown in Fig. 9.

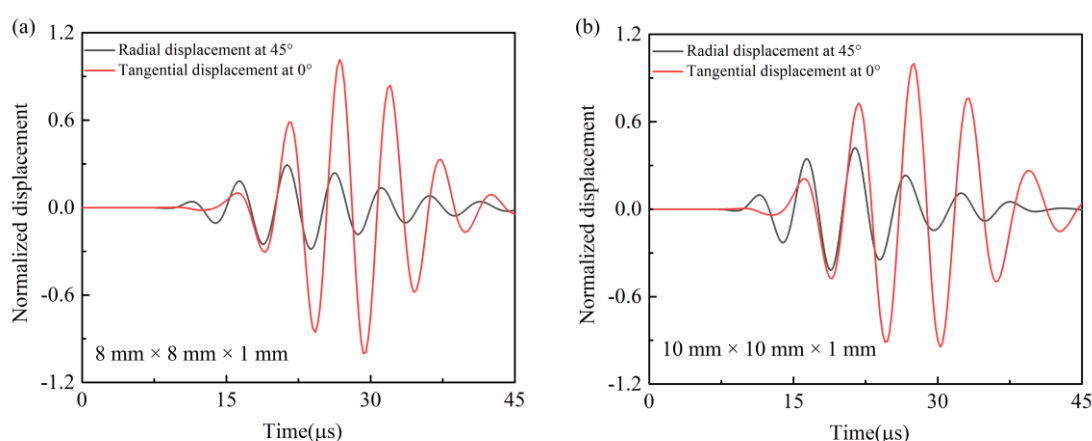


**Fig. 10** The FEM simulated displacement time history of guided waves excited by square face-shear  $d_{24}$  PZT wafers at 200 kHz with different dimensions. The plots are normalized against the maximum tangential displacement for each case.

From the above analysis it can be concluded that the size of the square face-shear transducer

should be small for high frequency  $SH_0$  wave generation. This conclusion is also reasonable if the dynamics of the PZT wafer is considered. For a square face-shear PZT wafer, the product of the resonance frequency  $f_r$  and the wafer length  $l$  is a constant, which is the well-known frequency constant  $N_{fs}$  [45]:

$$N_{fs} = f_r l. \quad (33)$$

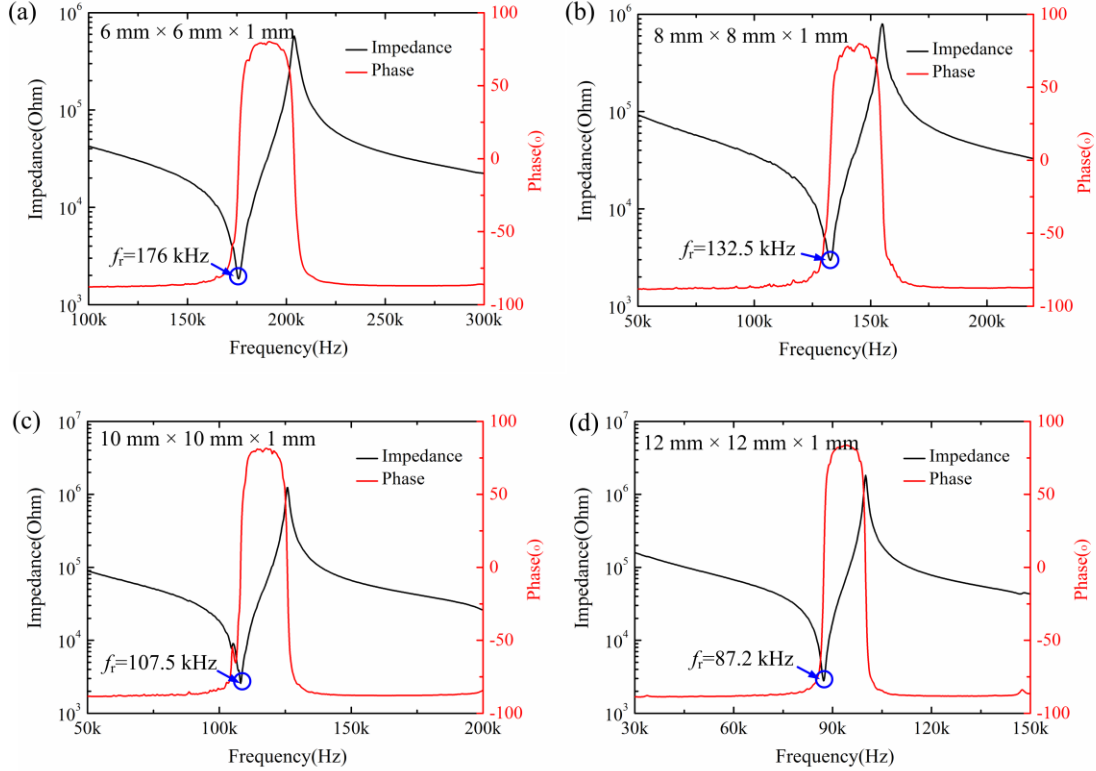


**Fig. 11** Impedance spectra of the face shear ( $d_{24}$ ) mode in square PZT-5H wafers with different dimensions.

In order to verify Eq. (33), an impedance analyzer (HIOKI, IM3570) is used to measure the  $d_{24}$  PZT wafer's impedance spectra, from which we can get the resonance frequency  $f_r$  of the face-shear mode[31]. As shown in Fig. 11, four sized square  $d_{24}$  mode PZT-5H wafers are investigated. By extracting the resonance frequency  $f_r$  of each PZT wafer (176 kHz for 6 mm long wafer, 132.5 kHz for 8 mm one, 107.5 kHz for 10 mm one and 87.2 kHz for 12 mm one), it is easy to find that the product of the resonance frequency  $f_r$  and the linear dimension  $l$  is almost a constant, which accords well with Eq. (33). As indicated in our previous work[36], a face-shear

transducer should work near its resonance frequency of the face-shear mode to get pure face-shear deformation and amplify the wave signal. Therefore, one can design the working frequency range by adjusting transducer's dimension. A small size transducer is preferred for high frequency  $SH_0$  wave excitation, which will not only decrease the unwanted Lamb wave at  $45^\circ$  direction but also exhibit high face-shear performance. Analogously, larger size transducer is suggested for low frequency  $SH_0$  wave excitation. For a given frequency range, one can determine the transducer size by using Eqs. (32) and (33).

### 5.2 The case of a bidirectional $SH_0$ wave piezoelectric transducer

The main advantage of the bidirectional  $SH_0$  wave piezoelectric transducer (BSH-PT) is to generate beam-focused  $SH_0$  wave[16], so it is very useful to obtain the analytical expression for the beam divergence angle for a BSH-PT. Referring to the bulk wave transducer, the beam divergence angle of the BSH-PT is defined as the deviate angle at which the amplitude of the  $SH_0$  wave field gets the first minima on either side of the main lobe, which are marked in Fig. 8. It can be seen from Eq. (27) that the wave field of the BSH-PT is only determined by a dimensionless function

$$R(k_2, L, W, \theta) = \left| \frac{[1 - \cos(k_2 W \sin \theta)] \sin(k_2 L \cos \theta) \cos(2\theta)}{k_2 L \sin(2\theta)} \right|. \quad (34)$$

If all parameters except  $\theta$  are kept constant, we can find the angle  $\theta_{\text{zero}}$  at which the dimensionless function  $R(k_2, L, W, \theta)$  gets the first minimum and the beam divergence angle  $\beta$  is then given by

$$\beta = \left| \theta_{\text{zero}} - \frac{\pi}{2} \right| = \begin{cases} \arcsin\left(\frac{\lambda}{2L}\right), & \frac{2L}{\lambda} > \sqrt{2} \\ \frac{\pi}{4}, & \frac{2L}{\lambda} \leq \sqrt{2} \end{cases}. \quad (35)$$

Obviously, the beam divergence is determined by the ratio of transducer's length  $2L$  to the wavelength  $\lambda$ . It can be seen from Eq. (34) that the amplitude of the  $SH_0$  wave is always zero at  $45^\circ$  direction. Therefore, when  $2L/\lambda \leq \sqrt{2}$ , the first minimum occurs at  $45^\circ$ , resulting in a constant beam divergence angle. Note that a divergence angle of  $45^\circ$  is too large for practice applications, so the effective length  $(2L/\lambda)$  of BSH-PT should be designed larger than  $\sqrt{2}$ .

When  $2L/\lambda > \sqrt{2}$ , the expression for the beam divergence angle  $\beta$  is the same as the corresponding expression for a Lamb wave interdigital transducer of length  $2L$ , where the beam divergence angle expression  $\arcsin[\lambda/(2L)]$  is calculated by a numerical model based on Huygens' principle[21]. Bearing in mind that the beam divergence angle for a bulk wave transducer of diameter  $2L$  is given by  $\arcsin[1.2\lambda/(2L)]$ , which is very similar to the obtained corresponding expression for BSH-PT, the difference is attributed to that the propagation of guided wave is two-dimensional, whereas that of the bulk wave is three-dimensional[21]. From Fig. 12, it can be seen that, for a given BSH-PT, narrow wave beam can be obtained by increasing the excitation frequency, while to design a transducer to excite a beam-focused  $SH_0$  wave with fixed wavelength, the length of the transducer should be as large as possible.

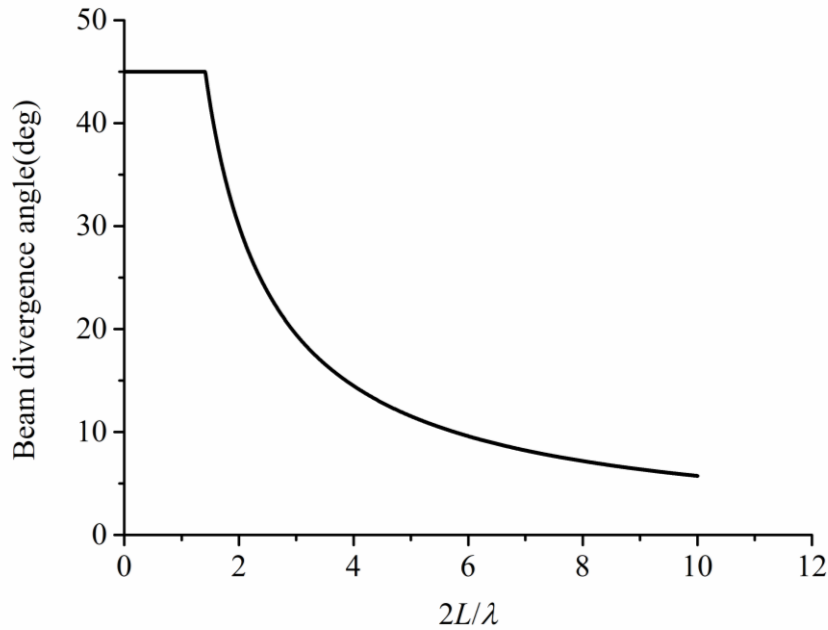


**Fig. 12** Theoretically predicated beam divergence angle as a function of the effective length ( $2L/\lambda$ ) of a bidirectional  $SH_0$  wave piezoelectric transducer.

Besides its length, the width of the bidirectional transducer can also be optimized. Based on Eq. (27), we can obtain the maximum amplitude of the excited  $SH_0$  wave as follow

$$|u_\theta(r_0, \theta)|_{\max} = \left| u_\theta(r_0, \frac{\pi}{2}) \right| = \left| \sqrt{\frac{2}{\pi k_2 r_0}} \varepsilon_{12}^{\text{const}} L [1 - \cos(k_2 W)] \right|. \quad (36)$$

If all the other parameters except  $L$  and  $W$  are kept constant, we obtain

$$|u_\theta(r_0, \theta)|_{\max} \propto L[1 - \cos(k_2 W)]. \quad (37)$$

Therefore, to maximize the amplitude of the generated  $SH_0$  wave,  $L$  should be also as large as possible. As for the width  $W$ , when it is given by

$$W = (2n+1) \frac{\pi}{k_2} = (2n+1) \frac{\lambda}{2}, \quad n = 0, 1, 2, 3, \dots \quad (38)$$

namely, the width  $W$  of the PZT wafer equals to odd multiple of the half wavelength  $\lambda/2$ , maximum  $SH_0$  wave is obtained. This is similar to the corresponding principle of Lamb wave PZT wafers[3, 14]. In practice applications, the value of  $W$  is suggested to be  $\lambda/2$  to minimize the power consumption. It should be noted that this optimization principle for  $W$  is only valid on the hypothesis that the dynamics of the transducer is neglected. If the dynamics of the transducer is considered, amplification by resonance should also be taken into account.

Based on the above analysis, it can be concluded that increasing the length of a transducer will not only decrease the beam divergence angle but also amplify the wave signal. However, bearing in mind that the BSH-PT shown in Fig. 3(a) is made up of two identical rectangular face-shear ( $d_{24}$ ) PZT wafers poled along its length direction. Note that the length of the PZT wafer cannot be too large in practice, since it is very difficult to pole a long wafer. Even for the soft PZT-5H ceramics, the manufacturing upper limit for length poling is typically about 30 mm. In order to overcome this contradiction, a new bidirectional  $SH_0$  wave piezoelectric transducer is proposed. As shown in Fig. 13, the proposed transducer is made up of four identical rectangular face-shear ( $d_{24}$ ) PZT wafers. This transducer can also be treated as a line array using two conventional BSH-PTs. Obviously, the length of proposed transducer can be further increased by adding the number of BSH-PTs in the array.

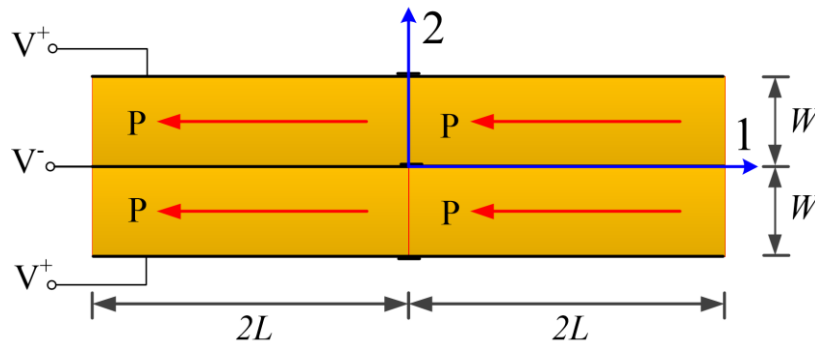


**Fig. 13** Schematics of the proposed bidirectional piezoelectric transducer for generating  $SH_0$  wave with narrow wave beam.

Experiments are then performed to explore the proposed transducer's performance on exciting  $SH_0$  wave with narrow wave beam. Four identical rectangular  $d_{24}$  PZT-5H wafers with dimensions of 24.8 mm×6.2 mm×1 mm are used to constitute the transducer. The experimental setup for measuring wavefield is the same as that introduced in Section 4. Fig. 14 (a) presents the comparison of the experimentally measured, theoretically predicated and FEM simulated  $SH_0$  wave fields in an aluminum plate generated by the proposed new bidirectional piezoelectric transducer at 250 kHz. It can be seen that experimental results are in good accordance with the theoretically predicated and FEM simulated ones, which confirms the validity of the proposed transducer. It should be noted that the beam divergence angle  $\beta$  for the generated  $SH_0$  wave of 250 kHz is only about  $14.5^\circ$ , which means that the wave beam is highly focused, as shown in Fig. 14(b). The proposed transducer will be very useful to excite circumferential shear horizontal waves in hollow cylindrical structures, in which narrow wave beam is especially desired[46].

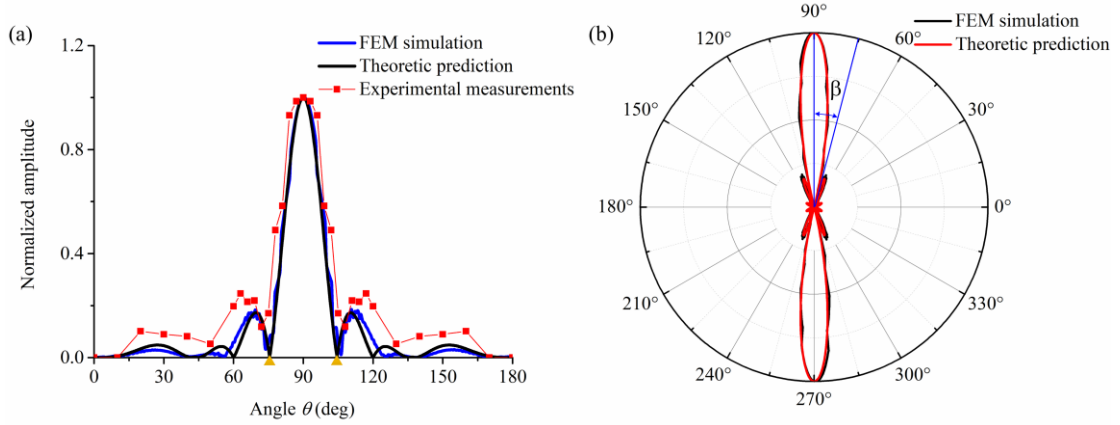


**Fig. 14** Comparison of the experimentally measured, theoretically predicated and FEM simulated  $SH_0$  wave fields in an aluminum plate generated by the proposed new bidirectional piezoelectric transducer at 250 kHz.

## 6. Summary and conclusions

In summary, based on the reciprocal theorem of elastodynamics and Huygens' principle, we proposed a theoretical model to solve the  $SH_0$  wave field generated by arbitrary-shaped face-shear transducers bonded on an infinite isotropic plate. It is found that the wave field generated by a face-shear transducer is equivalent to that generated by uniform in-plane tractions along its perimeter. Then this generic model is used to describe the wavefields for two specific cases of a

single square face-shear ( $d_{24}$ ) PZT wafer and a dual  $d_{24}$  PZT wafer based bidirectional  $SH_0$  wave piezoelectric transducer (BSH-PT). Simple analytical expressions for both cases were successfully obtained and validated by both FEM simulations and experimental tests. Furthermore, based on the obtained analytical expressions for the square face-shear PZT wafer and the BSH-PT, some general guidelines are derived to optimize the  $SH_0$  wavefield. For a square face-shear PZT wafer, it is suggested that a small size transducer is preferred for high frequency  $SH_0$  wave excitation. For the BSH-PT, to obtain narrow wave beam and maximize the wave signal, it is suggested that the length  $2L$  should be as large as possible and the width  $W$  equal to a half of the wavelength. Finally, based on these guidelines, a new bidirectional  $SH_0$  wave piezoelectric transducer is proposed and its capacity to excite pure  $SH_0$  wave with narrow wave beam is confirmed by experiments.

The proposed theoretical model is very simple and the obtained expression is analytical and explicit, so it can act as a guide for designers to optimize the face-shear transducer's parameters (such as transducer geometry, dimensions, excitation frequency, etc.) to control the radiation pattern of  $SH_0$  wave. Moreover, the model can also be used to guide the design of the magnetostrictive EMATs which can also generate the  $SH_0$  wave by inducing face-shear deformation in plates.

## Acknowledgments

We gratefully thank Dr. Jianghong Yuan (Southwest Jiaotong University, China) for his help on the theoretical framework.

## References

- [1] V. Giurgiutiu, Structural Health Monitoring with Piezoelectric Wafer Active Sensors, 2nd ed., Elsevier Academic Press, San Diego, CA, USA, 2014.
- [2] Z.G. Sun, B. Rocha, K.T. Wu, N. Mrad, A Methodological Review of Piezoelectric Based Acoustic Wave Generation and Detection Techniques for Structural Health Monitoring, International Journal of Aerospace Engineering, 2013 (2013) Article ID 928627, 22 pages.
- [3] V. Giurgiutiu, Tuned lamb wave excitation and detection with piezoelectric wafer active sensors for structural health monitoring, Journal of Intelligent Material Systems and Structures, 16 (2005) 291-305.
- [4] G.B. Santoni, L. Yu, B. Xu, V. Giurgiutiu, Lamb wave-mode tuning of piezoelectric wafer active sensors for structural health monitoring, Journal of Vibration and Acoustics-Transactions of the ASME,

129 (2007) 752-762.

- [5] B.L. Xu, V. Giurgiutiu, Single mode tuning effects on lamb wave time reversal with piezoelectric wafer active sensors for structural health monitoring, *Journal of Nondestructive Evaluation*, 26 (2007) 123-134.
- [6] E.V. Glushkov, N.V. Glushkova, O.V. Kvasha, R. Lammering, Selective Lamb mode excitation by piezoelectric coaxial ring actuators, *Smart Materials and Structures*, 19 (2010) 035018.
- [7] H. Kannajosyula, C.J. Lissenden, J.L. Rose, Analysis of annular phased array transducers for ultrasonic guided wave mode control, *Smart Materials and Structures*, 22 (2013) 085019.
- [8] J.P. Koduru, J.L. Rose, Time delay controlled annular array transducers for omnidirectional guided wave mode control in plate like structures, *Smart Materials and Structures*, 23 (2014) 105034.
- [9] C.M. Yeum, H. Sohn, J.B. Ihn, Lamb wave mode decomposition using concentric ring and circular piezoelectric transducers, *Wave Motion*, 48 (2011) 358-370.
- [10] Z. Su, L. Ye, Selective generation of Lamb wave modes and their propagation characteristics in defective composite laminates, *Proceedings of the Institution of Mechanical Engineers Part L-Journal of Materials-Design and Applications*, 218 (2004) 95-110.
- [11] Z. Liu, K. Sun, G. Song, C. He, B. Wu, Damage localization in aluminum plate with compact rectangular phased piezoelectric transducer array, *Mechanical Systems and Signal Processing*, 70-71 (2016) 625-636.
- [12] P. Kudela, M. Radzienski, W. Ostachowicz, Z. Yang, Structural Health Monitoring system based on a concept of Lamb wave focusing by the piezoelectric array, *Mechanical Systems and Signal Processing*, 108 (2018) 21-32.
- [13] L. Ambrozinski, T. Stepinski, P. Packo, T. Uhl, Self-focusing Lamb waves based on the decomposition of the time-reversal operator using time-frequency representation, *Mechanical Systems and Signal Processing*, 27 (2012) 337-349.
- [14] A. Raghavan, C.E.S. Cesnik, Finite-dimensional piezoelectric transducer modeling for guided wave based structural health monitoring, *Smart Materials and Structures*, 14 (2005) 1448-1461.
- [15] D.N. Alleyne, T. Vogt, P. Cawley, The choice of torsional or longitudinal excitation in guided wave pipe inspection, *Insight*, 51 (2009) 373-377.
- [16] H. Miao, Q. Huan, F. Li, G. Kang, A variable-frequency bidirectional shear horizontal (SH) wave transducer based on dual face-shear (d24) piezoelectric wafers, *Ultrasonics*, 89 (2018) 13-21.
- [17] M. Mańka, M. Rosiek, A. Martowicz, T. Stepinski, T. Uhl, PZT based tunable Interdigital Transducer for Lamb waves based NDT and SHM, *Mechanical Systems and Signal Processing*, 78 (2016) 71-83.
- [18] D.N. Alleyne, P. Cawley, Long range propagation of Lamb waves in chemical plant pipework, *Materials Evaluation*, 55 (1997) 504-508.
- [19] W.H. Zhu, J.L. Rose, Lamb wave generation and reception with time-delay periodic linear arrays: A BEM simulation and experimental study, *IEEE Transactions on Ultrasonics Ferroelectrics and Frequency Control*, 46 (1999) 654-664.
- [20] J.K. Lee, Y.Y. Kim, Tuned double-coil EMATs for omnidirectional symmetric mode lamb wave generation, *NDT & E International*, 83 (2016) 38-47.
- [21] P.D. Wilcox, P. Cawley, M.J.S. Lowe, Acoustic fields from PVDF interdigital transducers, *IEE Proceedings-Science Measurement and Technology*, 145 (1998) 250-259.
- [22] K.I. Salas, C.E.S. Cesnik, Guided wave excitation by a CLoVER transducer for structural health monitoring: theory and experiments, *Smart Materials and Structures*, 18 (2009).

- [23] Y.Y. Kim, Y.E. Kwon, Review of magnetostrictive patch transducers and applications in ultrasonic nondestructive testing of waveguides, *Ultrasonics*, 62 (2015) 3-19.
- [24] R. Ribichini, F. Cegla, P.B. Nagy, P. Cawley, Study and Comparison of Different EMAT Configurations for SH Wave Inspection, *IEEE Transactions on Ultrasonics Ferroelectrics and Frequency Control*, 58 (2011) 2571-2581.
- [25] C.F. Vasile, R.B. Thompson, Excitation of Horizontally Polarized Shear Elastic-Waves by Electromagnetic Transducers with Periodic Permanent-Magnets, *Journal of Applied Physics*, 50 (1979) 2583-2588.
- [26] R.B. Thompson, Generation of Horizontally Polarized Shear-Waves in Ferromagnetic Materials Using Magnetostrictively Coupled Meander-Coil Electromagnetic Transducers, *Applied Physics Letters*, 34 (1979) 175-177.
- [27] P. Wilcox, M. Lowe, P. Cawley, Lamb and SH wave transducer arrays for the inspection of large areas of thick plates, in: D.O. Thompson, D.E. Chimenti (Eds.) *Review of Progress in Quantitative Nondestructive Evaluation*, AIP Conf. Proc., New York, 2000, pp. 1049-1056.
- [28] P. Belanger, G. Boivin, Development of a low frequency omnidirectional piezoelectric shear horizontal wave transducer, *Smart Materials and Structures*, 25 (2016) 045024.
- [29] W.S. Zhou, H. Li, F.G. Yuan, Guided wave generation, sensing and damage detection using in-plane shear piezoelectric wafers, *Smart Materials and Structures*, 23 (2014) 015014.
- [30] H.C. Miao, F.X. Li, Realization of face-shear piezoelectric coefficient  $d_{36}$  in PZT ceramics via ferroelastic domain engineering, *Applied Physics Letters*, 107 (2015) 122902.
- [31] H.C. Miao, X. Chen, H.R. Cai, F.X. Li, Comparative face-shear piezoelectric properties of soft and hard PZT ceramics, *Journal of Applied Physics*, 118 (2015) 214102.
- [32] H.C. Miao, S.X. Dong, F.X. Li, Excitation of fundamental shear horizontal wave by using face-shear ( $d_{36}$ ) piezoelectric ceramics, *Journal of Applied Physics*, 119 (2016) 174101.
- [33] F.X. Li, H.C. Miao, Development of an apparent face-shear mode ( $d(36)$ ) piezoelectric transducer for excitation and reception of shear horizontal waves via two-dimensional antiparallel poling, *Journal of Applied Physics*, 120 (2016) 144101.
- [34] B. Kohler, T. Gaul, U. Lieske, F. Schubert, Shear horizontal piezoelectric fiber patch transducers (SH-PFP) for guided elastic wave applications, *NDT & E International*, 82 (2016) 1-12.
- [35] B.Y. Ren, H. Cho, C.J. Lissenden, A Guided Wave Sensor Enabling Simultaneous Wavenumber-Frequency Analysis for Both Lamb and Shear-Horizontal Waves, *Sensors*, 17 (2017) 488.
- [36] H.C. Miao, Q. Huan, F.X. Li, Excitation and reception of pure shear horizontal waves by using face-shear  $d(24)$  mode piezoelectric wafers, *Smart Materials and Structures*, 25 (2016) 11LT01.
- [37] H.C. Miao, Q. Huan, Q.Z. Wang, F.X. Li, A new omnidirectional shear horizontal wave transducer using face-shear ( $d(24)$ ) piezoelectric ring array, *Ultrasonics*, 74 (2017) 167-173.
- [38] Q. Huan, M.T. Chen, F.X. Li, A Comparative Study of Three Types Shear Mode Piezoelectric Wafers in Shear Horizontal Wave Generation and Reception, *Sensors*, 18 (2018) 2681.
- [39] J.S. Lee, Y.Y. Kim, S.H. Cho, Beam-focused shear-horizontal wave generation in a plate by a circular magnetostrictive patch transducer employing a planar solenoid array, *Smart Materials and Structures*, 18 (2009) 015009.
- [40] Q.Z. Ma, J.P. Jiao, P. Hu, X. Zhong, B. Wu, C.F. He, Excitation and Detection of Shear Horizontal Waves with Electromagnetic Acoustic Transducers for Nondestructive Testing of Plates, *Chinese Journal of Mechanical Engineering*, 27 (2014) 428-436.
- [41] P. Li, S. Shan, F. Wen, L. Cheng, A fully-coupled dynamic model for the fundamental shear

horizontal wave generation in a PZT activated SHM system, *Mechanical Systems and Signal Processing*, 116 (2019) 916-932.

[42] E.F. Crawley, J. de Luis, Use of piezoelectric actuators as elements of intelligent structures, *AIAA Journal*, 25 (1987) 1373-1385.

[43] A. Raghavan, C.E. Cesnik, Review of guided-wave structural health monitoring, *Shock and Vibration Digest*, 39 (2007) 91-116.

[44] A.C. Eringen, E.S. Suhubi, *Elastodynamics Volume 2 Linear Theory*, Academic press, New York San Francisco London, 1975.

[45] IRE Standards on Piezoelectric Crystals, in *Proceedings of the Institute of Radio Engineers*, 46 (1958) 764-778.

[46] R. Howard, F. Cegla, Detectability of corrosion damage with circumferential guided waves in reflection and transmission, *NDT & E International*, 91 (2017) 108-119.